

# X-ray polarization properties of thermal-radiative disc winds in binary systems

Ryota Tomaru <sup>1</sup>★, Chris Done <sup>1,2</sup> and Hirokazu Odaka <sup>3</sup>

<sup>1</sup>Centre for Extragalactic Astronomy, Department of Physics, Durham University, South Road, Durham DH1 3LE, UK

<sup>2</sup>Kavli Institute for Physics and Mathematics of the Universe (WPI), University of Tokyo, Kashiwa, Chiba 277-8583, Japan

<sup>3</sup>Department of Earth and Space Science, Graduate School of Science, Osaka University, 1-1 Machikaneyama, Toyonaka, Osaka 560-0043, Japan

Accepted 2023 November 22. Received 2023 November 22; in original form 2023 August 14

## ABSTRACT

New X-ray polarization results are challenging our understanding of the accretion flow geometry in black hole binary systems. Even spectra dominated by a standard disc can give unexpected results, such as the high-inclination black hole binary 4U 1630–472, where the observed X-ray polarization is much higher than predicted. This system also shows a strong, highly ionized wind, consistent with thermal-radiative driving from the outer disc, leading to speculation that scattering in the wind is responsible for the unexpectedly high polarization degree from a standard optically thick disc. Here, we show that this is not the case. The optically thin(ish) wind polarizes the scattered light in a direction orthogonal to that predicted from a standard optically thick disc, reducing about 2 per cent rather than enhancing the predicted polarization of the total emission. This value is consistent with the polarization difference between the disc-dominated soft state, where absorption lines by the wind are clearly seen, and the steep power-law state, where no absorption lines are seen. If this difference is genuinely due to the presence or absence of wind, the total polarization direction must be orthogonal to the disc plane rather than parallel as expected from optically thick material.

**Key words:** accretion, accretion discs–black hole physics–polarization–radiative transfer–stars: black holes–X-rays: binaries.

## 1 INTRODUCTION

The *Imaging X-ray Polarimetry Explorer* (*IXPE*; Weisskopf et al. 2016) has opened a new window for exploring the geometry of X-ray emission regions by detecting the net direction of the electric vector of the X-ray emission. A non-zero polarization implies a non-spherical geometry, e.g. an accretion disc. The classic result for a plane-parallel, optically thick, electron-scattering atmosphere (approximating a standard disc) gives a polarization degree (PD) of zero when viewed directly from above (as the source is symmetric when face-on) to 11.7 per cent for completely edge-on (Chandrasekhar 1960).

Emission from a disc around a black hole is affected by strong gravity. Geodesic transfer of the light rays rotates the plane of polarization, depolarizing the radiation from the innermost regions, which emit at the highest temperatures (Connors, Piran & Stark 1980; Dovčiak et al. 2008; Mikusincova et al. 2023), giving a diagnostic of black hole spin. This, plus the non-zero scale height of the outer disc, which blocks the highest inclination angles, means that the maximum PD expected from an accretion disc is of the order of 5–6 per cent.

*IXPE* observed the black hole binary (BHB) 4U 1630–472 (hereafter 4U 1630) in its recent outburst in 2022–2023 and detected strong polarization. The system parameters of this source are not well

known as it is at a large distance and is strongly absorbed (Kalemci, Maccarone & Tomsick 2018). None the less, the inclination can be estimated as  $65^\circ < i < 75^\circ$  from the combination of the presence of dips and the absence of eclipses (Kuulkers et al. 1998; Tomsick, Lapshov & Kaaret 1998). The high inclination is also implied by the detection of highly ionized absorption lines in its spectrum (Kubota et al. 2007; Díaz Trigo, Migliari & Guainazzi 2014; Neilsen et al. 2014; Hori et al. 2018; Gattuzz et al. 2019), which arise from the line of sight intercepting an equatorial disc wind (Ponti et al. 2012). Thus, we expect to see polarization from an accretion disc with PD of  $\approx 5$  per cent, potentially decreasing at the highest energies due to the general relativistic effects. Instead, the data show polarization increasing with energy from 6 per cent at 2 keV to 10 per cent at 8 keV (Kushwaha et al. 2023; Ratheesh et al. 2023; Rawat, Garg & Méndez 2023b, hereafter R23). This motivated speculation that the wind contributes to the observed polarization (Kushwaha et al. 2023; R23). The wind should give a polarization signal as it has a preferentially equatorial geometry from its disc origin and scatters some fraction of the incident flux.

In our previous work, we made a physical model of these winds from irradiation of the outer disc by the X-ray hot inner disc. The heated material expands and forms a wind driven by the pressure gradient for radii where the sound speed exceeds the escape velocity (thermal winds; Begelman, McKee & Shields 1983; Done, Tomaru & Takahashi 2018). We used a radiation-hydrodynamic code to calculate the geometry and kinematics of this material, also including

\* E-mail: [ryota.tomaru@durham.ac.uk](mailto:ryota.tomaru@durham.ac.uk)

the additional push by radiation pressure (thermal-radiative winds; Tomaru et al. 2019). We used the density/velocity structure as input to a Monte Carlo radiation transfer code, MONACO v1.6.0 (Odaka et al. 2011), to predict detailed line profiles, and showed that these matched well to those observed from both neutron star (Tomaru et al. 2020b, 2023b) and BHBs (Tomaru et al. 2020a). This includes the anomalous wind seen in the BHB GRO J1655–40, which was previously claimed to require magnetic driving but where the launch radius was underestimated due to the impact of radiative cascades and optical depth effects on the density diagnostic line (Tomaru, Done & Mao 2023a).

Here, we extend MONACO to handle polarization in radiation transfer and use this to explore the polarization properties of a thermal-radiative wind. We show that the wind *reduces* the total polarization, as scattering from the optically thin equatorial wind polarizes in the opposite direction (perpendicular to the disc plane, i.e. parallel to the spin axis) to that expected for the intrinsic disc emission (parallel to the disc plane; see e.g. Sunyaev & Titarchuk 1985, hereafter ST85), so the wind worsens the mismatch.

## 2 CALCULATING POLARIZATION IN MONACO

We use a Monte Carlo simulation code, MONACO (Odaka et al. 2011), for this study. This is a general-purpose framework for synthesizing X-ray radiation from astrophysical objects with complex geometry by calculating radiative transfer based on a Monte Carlo approach. It includes a full treatment of Comptonization from electrons with non-relativistic thermal and bulk motions, which is fully tested as described in Odaka et al. (2014).

We incorporate a new module to track photon polarization. We adopt the algorithm given by Matt et al. (1996) to calculate the polarization vector (a unit vector parallel to the electric field) of a Compton-scattered photon. We consider the scattering process of an initial photon in the electron’s rest frame of reference, so the observer’s frame is related to this frame through the Lorentz transformations. The photon energy  $E$ , direction  $\hat{\mathbf{k}}$ , and polarization vector  $\hat{\mathbf{e}}$  before (0) and after (1) scattering can be written as

$$(E_0, \hat{\mathbf{k}}_0, \hat{\mathbf{e}}_0) \rightarrow (E_1, \hat{\mathbf{k}}_1, \hat{\mathbf{e}}_1). \quad (1)$$

The degree of the polarization of the scattered photon is given by

$$p = \frac{2 - 2 \sin^2 \theta \cos^2 \phi}{\frac{E_1}{E_0} + \frac{E_0}{E_1} - 2 \sin^2 \theta \cos^2 \phi}, \quad (2)$$

where  $\theta$  and  $\phi$  denote the scattering and azimuth angles measured from the initial polarization vector  $\hat{\mathbf{e}}_0$ , respectively. The polarization vector  $\hat{\mathbf{e}}_1$  of the scattered photon is assigned to be

$$\hat{\mathbf{e}}_1 = \frac{1}{A_1} \hat{\mathbf{k}}_1 \times (\hat{\mathbf{e}}_0 \times \hat{\mathbf{k}}_1) = \frac{1}{A_1} (\hat{\mathbf{e}}_0 - (\hat{\mathbf{e}}_0 \cdot \hat{\mathbf{k}}_1) \hat{\mathbf{k}}_1), \quad (3)$$

$$A_1 = |\hat{\mathbf{k}}_1 \times (\hat{\mathbf{e}}_0 \times \hat{\mathbf{k}}_1)|, \quad (4)$$

with a probability equal to the polarization fraction  $p$ ;  $A_1$  is merely the size of the calculated vector for normalization. Otherwise, the photon is depolarized with a probability of  $1 - p$ ; therefore, the polarization vector is assigned to be randomly sampled. This treatment results in unpolarized photons after a number of Monte Carlo trials.

We first demonstrate the performance of the polarization module in MONACO by showing results for electron scattering in a constant-density plane-parallel slab with optical depth from  $\tau = 0.5$  to 8 (see Fig. 1) to compare with the classic paper of ST85. ST85 assumed Thompson scattering (no electron energy change) of seed photons

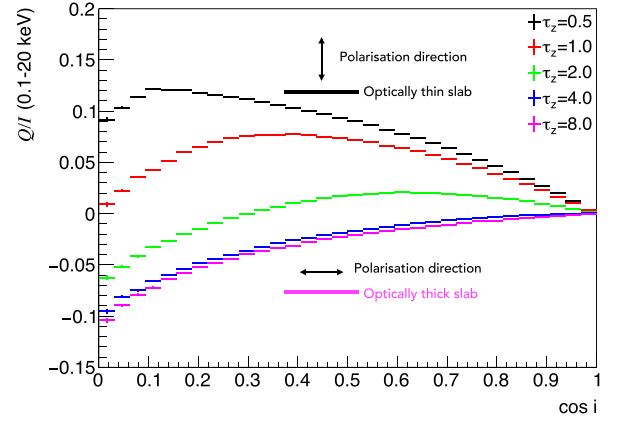


**Figure 1.** The PD produced by electron scattering from a slab of different optical depths. This matches the results of ST85, though we caution that they use the opposite sign convention. We have included sketch geometries to make it clear that the polarization expected from a standard optically thick disc is aligned along the disc plane (defined as negative). In contrast, the polarization expected from an optically thin slab is perpendicular to the disc, i.e. aligned with the radio jet (defined as positive).

with energy  $\ll kT_e$ , but MONACO always includes the full Compton scattering cross-section. We set the seed photons as a blackbody distribution at the radiation temperature ( $kT_e = kT_{bb} = 1$  keV) so that up-scattering and down-scattering cancel after multiple events. We emit  $4 \times 10^8$  seed photons isotropically on the mid-plane of the slab to compare to geometry (a) in ST85. We use  $-1 < \cos i < 1$  for all computations but only show the  $0 < \cos i < 1$  in all figures due to the symmetry in this paper.

Fig. 1 shows the resulting polarization (Stokes parameters  $Q/I$  as  $U = 0$  due to axisymmetry) as a function of inclination. These are integrated over the entire spectrum to compare directly with ST85 (their fig. 6a). However, we use the opposite sign convention here, so that the positive  $Q$  direction is normal to the disc (or slab) plane, as shown by the inset sketch geometries. This sign convention is the same as Chandrasekhar (1960). Our results match well with ST85, demonstrating that the polarization is calculated correctly, with the highest optical depths tending towards the classical Chandrasekhar (1960) result, while lower optical depths have lower polarization, which changes sign as the scattering medium goes optically thin.

Physically, the change in the sign of polarization is due to the corresponding change in the direction of the photons before their final scattering. In an optically thick slab, the photons are all diffusing upwards, so they have fairly uniform momentum vectors perpendicular to the plane. Hence, they have an electric vector, which is parallel to the plane. Electron scattering tends to preserve the plane of the electric vector, so the photon resulting from the final scattering also has an electric vector parallel to the plane of the slab (defined as a negative sign on  $Q$ ). By contrast, in the optically thin slab, photons scattered by an electron are more likely to be moving parallel to the plane of the slab as they are the ones that encounter the largest optical depth and have the largest probability of being scattered. These can have a range of azimuthal angles with respect to the observer. Those which are at an azimuth of 0 (directly towards) or 180 (directly away) will have electric vectors before (and after) scattering in the plane of the slab, but the majority are at other azimuths, which gives a net electric vector perpendicular to the slab plane (positive polarization; Angel 1969).

This switch in polarization direction with optical depth is important to understand what is expected from BHBs as they show a state

transition, from being dominated by an optically thick, geometrically thin disc (high/soft state) to the low/hard state where the emission is instead dominated by Comptonization by hot ( $\sim 100$  keV), optically thin plasma. If this hot accretion flow has a disc-like geometry, then this predicts that the state transition accompanies a change in the sign of the polarization, with the high/soft state polarization aligned with the plane of the disc, which is perpendicular to the jet, to the low/hard state aligned perpendicular to the plane of the disc, which is parallel to the jet. We note that the net polarization predicted for the hot flow will be smaller than that calculated in Fig. 1 due to the larger energy change in inverse Compton scattering in the hot ( $\sim 100$  keV) flow, which reduces the polarization (equation 2) compared to that calculated here for electrons at 1 keV.

*IXPE* has observed a low/hard state in the BHB Cyg X-1 (Krawczynski et al. 2022). To zeroth order, this follows the expectations above for an optically thin(ish) flow in a disc geometry in that the polarization is aligned with the jet (i.e. perpendicular to the disc). This rules out multiple other geometries where the optically thin material is a compact source on the spin axis (almost no polarization) or aligned along the jet direction (polarization with the wrong sign), though a more detailed understanding of the polarization and hence source geometry is still missing (Krawczynski et al. 2022; Veledina et al. 2023; Zdziarski et al. 2023). We note that very similar polarization, aligned with the jet, is seen in the low Eddington fraction active galactic nucleus NGC4151 (Gianolli et al. 2023), where the accretion flow is likely to be similar to the low/hard state in BHBS (Kubota et al. 2018; Mahmoud & Done 2020).

By contrast, the disc-dominated state is expected to have polarization parallel to the disc plane, i.e. perpendicular to the jet direction. However, this expected switch has not been seen in the soft state of Cyg X-1; instead, the polarization direction is consistent with that of the hard state, which is parallel to the jet axis, and its magnitude is  $\sim 2$  per cent (Dovciak et al. 2023). It is not clear whether this is typical for disc-dominated states in general. Cyg X-1 may be a special case as it never makes a very clean transition to the disc-dominated state (Done & Gierliński 2005; Sugimoto et al. 2016). This could be due to it never quite reaching high enough luminosity to make a full transition or that there is always some component of wind-fed accretion from the high-mass companion star, which prevents the disc from forming.

These results already show that optically thin scattering by a wind is likely to depolarize the total emission from an optically thick accretion disc as they give opposite polarization directions. We explore this further below, using a physical model for the wind in the high/soft state of 4U1630.

### 3 POLARIZATION FROM A WIND

#### 3.1 The wind model

Thermal-radiative winds depend on the spectral shape (setting the radiation temperature), total luminosity (setting the heating rate and radiation pressure), and disc size (e.g. Done et al. 2018). Only the first of these is securely known from the data for 4U1630, as the high optical extinction prevents observations of the companion star, so neither distance nor orbit is known.

Instead, we use our previous the radiation-hydrodynamical (RHD) simulation from the similarly highly inclined neutron star binary GX13+1 (Tomaru et al. 2020b). This has similarly large equivalent widths in highly ionized iron absorption lines to those seen in 4U1630 [ $\sim 50$  eV for Fe XXVI, and 25–30 eV for Fe XXV (Gatuzz et al. 2019) and Allen et al. (2018)], so we use this wind as the basis of our

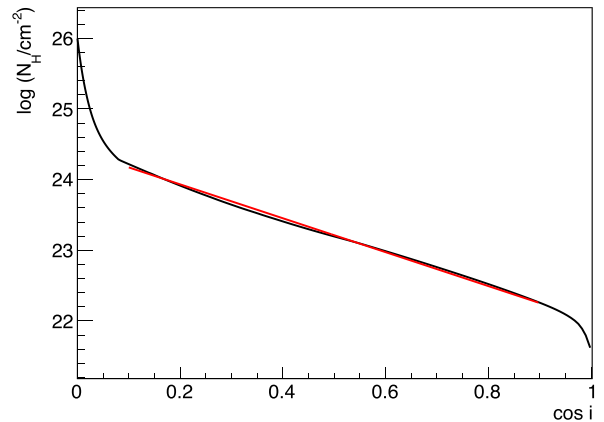


**Figure 2.** The comparison between column density of the accretion disc wind from the RHD simulation (black) and the analytical fitting formula (red). The disc equatorial plane is at  $\cos i = 0$ .

polarization calculation. This simulation has Compton temperature  $T_{IC} = 1.3 \times 10^7$  K, giving a Compton radius (where the typical thermal speed of the particles exceeds the local escape velocity) of  $R_{IC} = 0.61 m_p GM / (kT_{IC}) \sim (6 \times 10^5 / T_{IC,7}) R_g$ , where  $T_{IC,7} = T_{IC} / 10^7$  K. Other important parameters are luminosity  $L = 0.5 L_{Edd}$  and outer disc radius  $10 R_{IC}$ .

Fig. 2 shows the resulting column density of the radiation-hydrodynamic simulation as a function of viewing angle (black; from fig. 2 in Tomaru et al. 2020b). This can be well described by an analytical fitting function  $\log(N_H(\mu)/\text{cm}^{-2}) = 22 + 2.4(1 - |\mu|)$  in the range of  $0.1 < |\mu| < 0.9$ , where  $\mu = \cos i$  (Fig. 2; red line). This is a typical column density distribution in the thermal wind models, giving a much better description of the radiation-hydrodynamic results than the  $N_H \propto (1 - |\mu|)$  assumed in Done et al. (2018). The system parameters of 4U1630 are probably rather similar in terms of Compton temperature, luminosity, and  $R_{out}/R_{IC}$ , so the wind should also be similar.

We make an analytical approximation to this density distribution,  $n(R, \mu)$ , such that

$$n(R, \mu) = N_H(\mu) \frac{R_{in} R_{out}}{(R_{out} - R_{in}) R^2}, \quad (5)$$

where the  $n \propto R^{-2}$  dependence comes from the launch condition for thermal winds (Done et al. 2018).

We sample this density structure on a logarithmic radial grid ( $\Delta R/R$  constant; 8 bins from  $R_{in} - R_{out}$  of  $0.1 - 1 R_{IC}$ , where the outer disc radius is smaller than the original RHD simulation to reduce computational cost), and a constant solid angle polar grid ( $\Delta \mu$  constant; 32 bins from  $\mu = 0.01 \rightarrow 1$ , with another 32 from  $\mu = -0.01 \rightarrow -1$ ) and uniform grid of  $\Delta \phi$  (32 bins;  $0 \rightarrow 2\pi$ ). We put  $\tau = 5$  between  $\mu = 0.01$  and the mid-plane so that photons cannot cross from the lower half to the upper half plane. The resultant density distribution is shown in Fig. 3.

#### 3.2 Wind scattering of unpolarized input photons with different angular distributions

The wind in the radiation-hydrodynamic simulation is set self-consistently by the radiation field. In particular, the wind structure can change for different illumination patterns. However, the wind in GX 13+1 is marginally optically thick, so this probably represents the strongest wind that can be seen as any further increase in illumination to increase the wind column density will start to shield

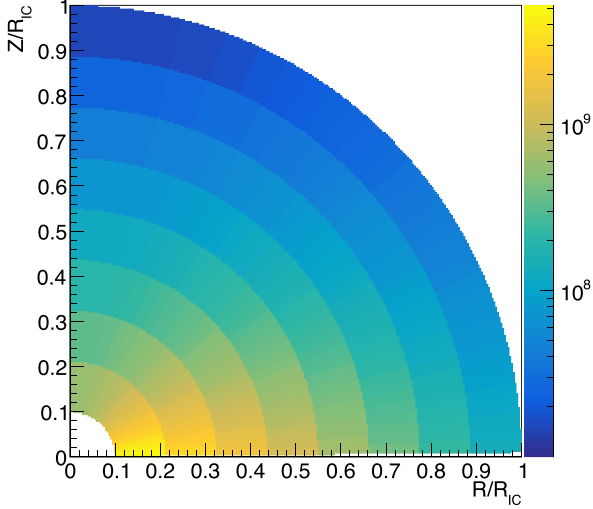


**Figure 3.** The density distribution calculated by equation (5).

the disc. Hence, we take this wind structure as static and explore how scattering in the wind imprints a polarization signal on intrinsically unpolarized flux.

We consider three different illumination patterns, one where the photons from the inner disc are isotropic, so  $L(\mu) = L_0$ , one where  $L(\mu) = 2\mu L_0$  (absorption-dominated atmosphere), and one where  $L(\mu) = \mu(1 + 1.8\mu)L_0/1.1$  (electron scattering; ST85), where  $L_0$  is the mean (angle-integrated) luminosity in all cases. These different polar angle flux distributions give different amounts of incident flux with the angle of the wind. The isotropic distribution is probably most appropriate for the bright neutron star binaries, where there is a boundary layer as well as the disc. The electron-scattering pattern is the one expected for a disc above 1.2–1.5 keV where there is little true absorption opacity (Davis, Done & Blaes 2006), but Doppler boosting affects the illumination from a Keplerian disc, giving a pattern that is closer to the absorption-dominated one. These three illumination patterns then span the range expected for all the bright low-mass X-ray binary (LMXB) systems. We use the same Monte Carlo simulation for all three but weigh the photons differently for each illumination pattern. Hence, the Poisson errors are correlated in all three cases.

Fig. 4 shows the polarization of the scattered flux for the three illumination patterns. The isotropic point source gives scattered flux, which is more polarized than the disc illumination patterns, as the isotropic source has more illumination of the equatorial parts of the wind, which are at the highest inclination angles. The degree of polarization decreases as the illumination becomes more polar, as it picks out higher parts of the wind, which are less inclined. However, the most important point is that all the scattered fluxes are polarized in the same (positive) direction, i.e. polarized perpendicular to the plane of the disc.

The scattered emission dominates in the subset of sources where the much brighter direct emission is obscured by the disc itself. These are the accretion disc corona sources, such as 2S0921 (Tomaru et al. 2023b). These results predict that these sources should be strongly polarized and with a PD, which gives a diagnostic of the angular distribution of the intrinsic source illumination pattern.

However, in 4U1630, we see the intrinsic (primary) emission directly, so the expected polarization from the scattered emission is diluted. The sum of two components, each with Stokes parameters of  $I_p, Q_p$  and  $I_s, Q_s$  (where  $I$  is equivalent to the number of photons),

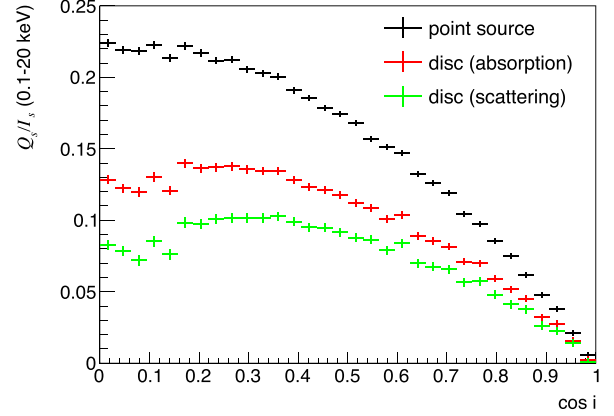


**Figure 4.** The PD from scattering in the wind for the three different illumination patterns. Isotropic scattering has the largest number of photons illuminating the highest inclination material, so it has a larger polarization than the disc-like (either absorption or electron-scattering) illumination patterns. Importantly, all these polarizations have a positive sign, i.e. the polarization is perpendicular to the plane of the disc.

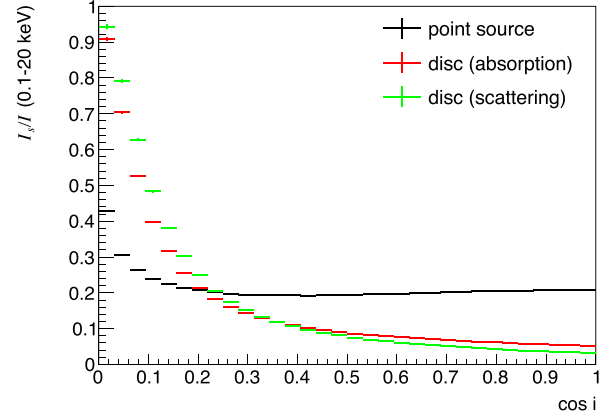


**Figure 5.** The ratio of the wind scattered to total (scattered plus absorbed primary) flux seen in any direction for the three illumination patterns. Absorption of the primary component in the wind at high inclination means that the scattered flux becomes increasingly important. This is especially marked in the disc-like illumination patterns, as the primary flux is intrinsically low in the equatorial plane.

gives  $Q/I = (Q_p + Q_s)/(I_p + I_s) = (Q_p/I_p) \times I_p/I + (Q_s/I_s) \times I_s/I$ . Here, we assume that the intrinsic emission is unpolarized, so  $Q_p = 0$ . Hence,  $Q/I = Q_s/I_s \times I_s/I$ , where  $I = I_p + I_s$  and  $I_p = L(\mu)\exp(-\tau_\mu)$ , where  $\tau_\mu = 1.2\sigma_T N_H(\mu)$ , i.e. includes the electron-scattering losses for a direct line of sight through the column. Fig. 5 shows the ratio  $I_s/I$  as a function of the angle for each source illumination pattern. The scattered emission makes up over 20 per cent of the total emission for the isotropic source but is much less for the disc-like illumination patterns. This is because the isotropic source has more illumination of the equatorial parts of the wind, which are the most optically thick, producing more scattered flux.

We can estimate the fraction of scattered flux analytically from  $I_s = \int_{\phi=0}^{2\pi} \int_{\mu=0}^1 L(\mu)(d\Omega/2\pi)\tau_\mu$ . These integrate to  $0.3L_0, 0.1L_0$ , and  $0.08L_0$ , respectively, so  $I_s/I_p = 0.3, 0.05/\mu$ , and  $0.088/[\mu(1 + 1.8\mu)]$  in the regions where absorption is negligible, i.e.  $\mu \geq 0.5$ . (The attenuation of primary component is negligible because it is the optically thin.) This gives a good match to the simulated ratios in Fig. 5, in particular predicting  $I_s/(I_p + I_s) = I_s/I = 0.23$  for the

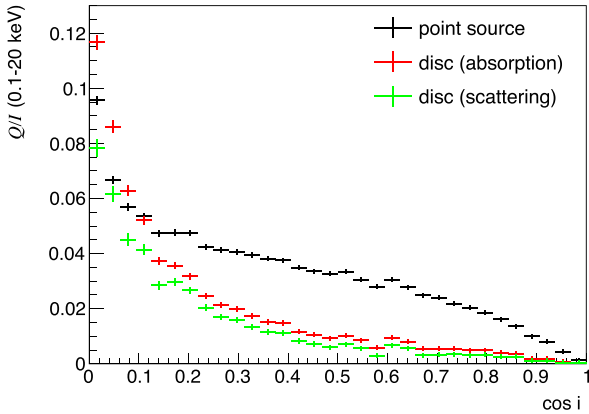


**Figure 6.** The PD of the total spectrum due to scattering in the wind for the three different (unpolarized) illumination patterns. This is derived from the combination of the polarization of the scattered flux (Fig. 4) diluted by the ratio of scattered to total flux (Fig. 5). All the resultant polarizations are in the positive direction (perpendicular to the plane of the disc), as the scattered flux is the only polarized component.

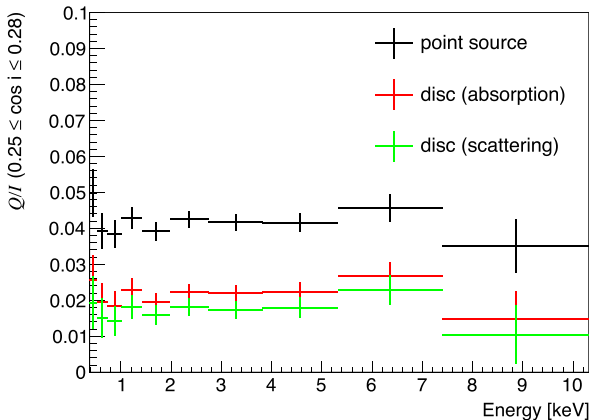


**Figure 7.** The PD of the total spectrum as a function of energy for the three different (unpolarized) illumination patterns. Each one is constant as the electron-scattering cross-section is constant with energy.

isotropic case, as observed at  $\mu \geq 0.5$ . The increase in optical depth for lower  $\mu$  suppresses the direct component, increasing the scattered flux's contribution. The decrease in direct component normalization is even more marked with the disc-like illumination patterns, as these have intrinsically less flux at high inclination angles, so the scattered flux dominates more.

We combine the ratio of scattered flux,  $I_s/(I_s + I_p)$  (Fig. 5), with the PD of the scattered photons (Fig. 4) to derive the total polarization in Fig. 6. This is lower for the more realistic disc-like illumination patterns, both because of the lower intrinsic PD of the scattered emission (Fig. 4), and their lower contribution of the scattered to total emission (Fig. 5).

Fig. 7 shows the (lack of) energy dependence of this polarization signal for  $\mu = 0.25$ . This is expected as the simulated wind is completely ionized, so the scattering has no energy dependence.

### 3.3 Wind scattering of intrinsically polarized accretion disc photons

The disc spectrum should be intrinsically polarized from its predominantly electron-scattering, plane-parallel atmosphere. We replace the

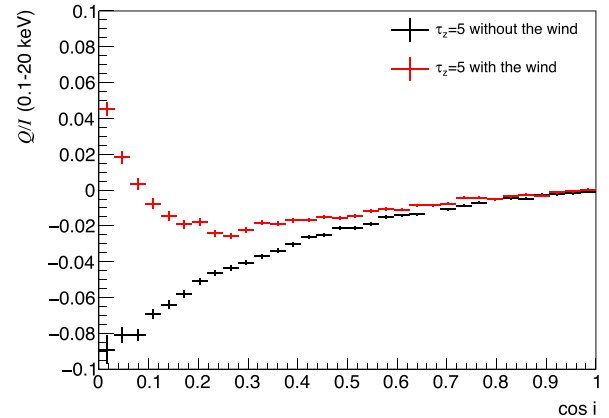


**Figure 8.** Polarization from the disc (black) as a function of angle, compared to polarization from disc plus wind (red). The wind reduces the polarization signal as the optically thin wind switches the direction of the electric vector compared to the optically thick disc (see Fig. 1).

unpolarized blackbody source used above with a thin disc structure in MONACO. This has isotropic seed photons on the mid-plane with  $T(R) = T_{\text{in}}(R/R_{\text{in}})^{-3/4}$  where  $T_{\text{in}} = 1.5$  keV and  $R_{\text{in}} = 6R_g$  ( $R_g = GM/c^2$ ) to match the data. This is overlaid by an electron-scattering atmosphere with  $\tau = 5$  and  $T_e(R) = T(R)$  to give both the electron-scattering radiation pattern and PD. This is shown in black in Fig. 8, and matches well to the theoretical Chandrasekhar result. This shows that the multitemperature disc gives the same result as the constant-temperature slab of Fig. 1. We also confirmed that the angle dependence of this illumination is as expected for an electron-scattering atmosphere.

The red points show the result when this polarized spectrum with its electron-scattering angle-dependent illumination pattern scatters off the wind. The polarization of the total (scattered plus direct) emission is strongly reduced by the orthogonal direction of the scattered polarization, so the total polarization (wind scattering plus disc) at  $\mu = 0.25$  ( $\sim 75^\circ$ ) decreases from 5 per cent to around 3 per cent. This is much smaller than the 6–10 per cent measured in 4U1630, showing that scattering in the wind is not a viable way to increase the polarization signal from a standard disc.

## 4 FITTING HIGH/SOFT STATE DATA FROM 4U1630

There is one more effect that we have not yet included, which is that the wind is not actually completely ionized as it has strong absorption lines from H- and He-like iron imprinted on it. This will suppress the direct flux at these energies, increasing the importance of the scattered flux and hence increasing the polarization.

We use one of the data sets (ObsID: 5501010107) taken by Neutron Star Interior Composition Explorer (NICER), which was simultaneous with the *IXPE* observation to assess the impact of this. We fit this in XSPEC with a model where an intrinsic simple disc spectrum (`diskbb`) is absorbed by the wind. We calculate this using `pion` in SPEX v3.06.01 (Kaastra, Mewe & Nieuwenhuijzen 1996; Mao et al. 2017). We illuminate solar abundance material by a disc spectrum (the `Dbb` model in SPEX with temperature of 2 keV, which is equivalent to `ezdiskbb` with 1 keV in XSPEC) and tabulate the results as a multiplicative model (`mtable`). This includes the effects of both absorption by ionic lines/edges and attenuation by electron scattering. If the direct spectrum was the only component, then this could be modelled as `mtable{ pion.fits }*diskbb`, but

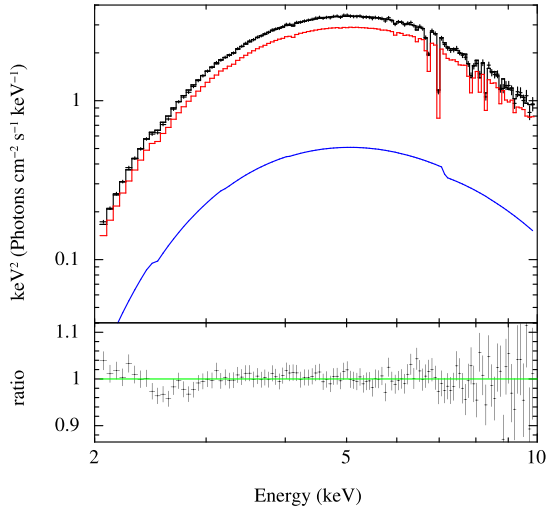


**Figure 9.** The upper panel shows the *NICER* data (black points) fit in the 2–10 keV band by a `diskbb` continuum, which is seen directly through the highly ionized absorber (red) and via scattering (blue). See Table 1 for the model parameters. The lower panel shows the ratio of the model to the data, showing that the fit is generally very good.

there is also the scattered component from the wind. We include this by using a covering fraction,  $f_{\text{cov}}$ , so that the scattered spectrum is normalized by  $1 - f_{\text{cov}}$ . Hence, the ratio of scattering to total flux is given by

$$\frac{I_s}{I_s + I_p} = \frac{1 - f_{\text{cov}}}{1 - f_{\text{cov}} + f_{\text{cov}} \exp(-\tau)}. \quad (6)$$

All these components are affected by interstellar absorption, modelled with (`tbabs`). The total model is `tbabs*(partcov*table{ pion.fits })*diskbb`.

We fit this to the 2–10 keV bandpass, ignoring the lower energy data as this is heavily absorbed and affected by the dust scattering in the interstellar medium along the line of sight (Kalemci et al. 2018). The lower energy band data do not affect the fitting of the ionized absorption, which is of most interest here.

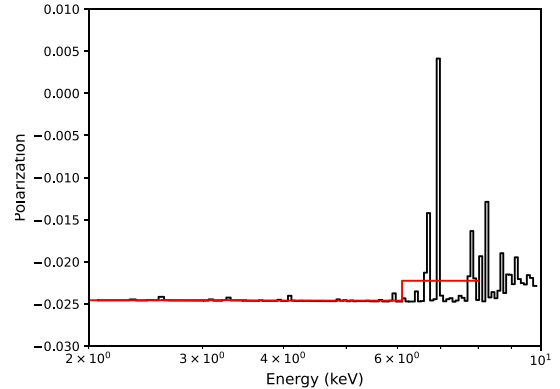
Fig. 9 shows this best-fitting model fit to the *NICER* data, with the direct ( $I_p$ , red with absorption features) and scattered ( $I_s$ , blue) contributions separated out as in equation (6). The scattered component is not significantly detected (uncertainty on  $f_{\text{cov}}$  includes 1), but there is a strong prediction that high spectral resolution microcalorimeter data from upcoming missions such as *X-Ray Imaging and Spectroscopy Mission (XRISM)* and *newAthena* should see these strong absorption lines with non-zero flux at the line centre due to the contribution of the scattered emission.

Table 1 shows the best-fitting parameters. The disc temperature is almost identical to that seen in the *IXPE* observations (R23). The column density is almost exactly the same as predicted by our wind model, where the column along the line of sight at  $75^\circ$  ( $\mu \sim 0.25$ ) is  $6 \times 10^{22} \text{ cm}^{-2}$  ( $N_{\text{H}} = 10^{22 + 2.4 \times 0.75}$ ). This corresponds to  $\tau = 0.5$ . The fraction of scattered to total flux is  $0.11^{+0.09}_{-0.11}$ . The best-fitting value indicates  $\mu \sim 0.35$ , but the error range includes our predicted ratio of  $\sim 0.15$ – $0.2$  at  $\mu = 0.25$  (Fig. 5). Thus, our wind simulation agrees with the estimated scattered flux contribution in the data.

We fix the wind covering fraction and column to that of the simulation and estimate the additional suppression of the primary

**Table 1.** Spectral fit to the 2–10 keV *NICER* data. The pion wind absorption has turbulent velocity fixed at  $200 \text{ km s}^{-1}$  and illuminating spectrum similar to a 1 keV `diskbb`. The fit has  $\chi^2/\text{dof} = 84/110$ .

Model	Parameter	Value
<code>tbabs</code>	$N_{\text{H}}/10^{22} \text{ (cm}^{-2}\text{)}$	$7.82 \pm 0.04$
<code>partcov</code>	$f_{\text{cov}}$	$0.93 \pm 0.07$
<code>pion</code>	$N_{\text{H}}/10^{22} \text{ (cm}^{-2}\text{)}$	$60 \pm 15$
	$\log_{10}(\xi/\text{(erg cm s}^{-1}\text{)})$	$5.37 \pm 0.08$
	$v_{\text{out}} \text{ (km s}^{-1}\text{)}$	$840 \pm 400$
<code>diskbb</code>	$kT \text{ (keV)}$	$1.51 \pm 0.01$
	Norm	$230 \pm 30$



**Figure 10.** The black line shows the predicted PD of the total spectrum shown in Fig. 9 as a function of energy assuming that the electron-scattering-dominated disc's intrinsic polarization is  $-0.05$  and the scattered-flux polarization is  $+0.10$ . The increased importance of scattered flux in the absorption lines leads to the jump in polarization at these energies, but when binned to the *IXPE* resolution (red) the effect is very small.

flux due to the absorption lines, and hence the increase in the fraction of scattered flux in the lines. At  $\mu = 0.25$ , the scattered emission has polarization of  $0.10$  while the direct flux seen from the electron-scattered disc has PD of  $-0.05$ . We calculate the expected polarization as a function of energy using the *NICER* data resolution (black line in Fig. 10). This clearly shows the increase in the absorption line energies due to the increase in scattered fraction at these energies. However, the number of photons in the lines is quite small, so binning up to the *IXPE* resolution (red line) gives only a very small effect on the total polarization signal as a function of energy. We predict that the polarization remains almost constant with energy at PD of around  $0.02$ , which is incompatible with the observed PD, which linearly increases from 6 per cent to 11 per cent from 2 to 8 keV (Ratheesh et al. 2023).

## 5 STEEP POWER-LAW STATE OF 4U1630

*IXPE* also observed 4U1630 in a steep power-law (SPL) state, where the observed luminosity is three to four times higher than that seen in the disc-dominated data (Rawat, Garg & Méndez 2023a; Rodriguez Cavero et al. 2023). There are no wind absorption features seen in the simultaneous *NICER* data for these data (Rodriguez Cavero et al. 2023), nor in past observations of the source in this state (Hori et al. 2018; Gatuzz et al. 2019; Trueba et al. 2019). The increase in Compton temperature and ionization parameter from the spectral change is not in itself enough to make the wind completely ionized and hence invisible in absorption (Gatuzz et al. 2019; see

also Shidatsu & Done 2019), but we note that the luminosity is likely super-Eddington, so radiation pressure may change the wind structure dramatically, perhaps making it much faster (hence less dense) and/or more equatorial (so smaller solid angle to scattering).

If the wind column and/or opening angle has really decreased, then the polarization signal from the wind-scattered component should also decrease. In the limit where the wind disappears, this gives a predicted drop of PD of 0.02. We note that this is exactly the observed change in polarization between the high/soft and SPL states (Rodríguez Cavero et al. 2023), though this would also require that there is no change in intrinsic source polarization between the two very different spectra. If the difference in polarization is genuinely due to the presence or absence of the wind, then the intrinsic disc polarization must be perpendicular to the disc plane rather than parallel to the disc plane as expected from electron scattering.

## 6 WIND POLARIZATION IN NEUTRON STAR LMXRB

We can calculate the expected wind column density using the RHD code for any spectral shape, luminosity, and disc size. The column should scale as  $\propto L \log R_{\text{out}}/0.1R_{\text{IC}}$  (Hori et al. 2018) up to the point where the winds self-limit by becoming optically thick along the equatorial plane (as simulated here) and/or the luminosity goes super-Eddington (at which point the structures become highly uncertain).

Neutron star binaries should have similar accretion discs to the black hole systems but with the addition of a bright boundary layer between the disc and solid neutron star surface. So far, *IXPE* has observed only two soft state neutron star systems with  $L < L_{\text{Edd}}$ , namely GS 1826–238 (Capitanio et al. 2023) and GX 9+9 (Ursini et al. 2023). These are very short period (i.e. small disc) systems, so they should have very weak winds. The contribution of the wind to the polarization signal should be negligible.

Strong winds are seen in some neutron star systems, but *IXPE* has not yet observed these. Strong blueshifted, highly ionized absorption lines are seen in the bright, high-inclination, large-disc system, GX 13+1. Our wind structure was directly calculated from this system, so our results predict the polarization signal from the wind. This should be energy-dependent as the spectrum is dominated by the disc at lower energies (2–3 keV), switching to the boundary layer above this. The boundary layer is more isotropic, so Fig. 7 predicts that this should carry a wind polarization signal of PD  $\sim 0.04$ , while the disc carries a signal with PD  $\sim 0.02$ .

The other large-disc neutron star binary is S0921. Here, the system is viewed at such a high inclination that the outer disc blocks the direct emission. The source is seen only via scattering in the wind, with emission lines from the highly ionized wind material dominant over absorption (Tomaru et al. 2023b). All the spectrum is seen via scattering, so this predicts that the polarization should increase with energy from  $\sim 0.1$ , where the disc illumination pattern dominates (below 3 keV), to  $\sim 0.2$ , where the more isotropic boundary layer dominates (see Fig. 4). These predictions are testable with future *IXPE* observations, and this should enable the wind polarization to be separated from any intrinsic polarization of the disc and boundary layer.

## 7 CONCLUSIONS

Black hole X-ray binaries in their disc-dominated state can be well fitted by simple (sum of blackbody) models of an optically thick, geometrically thin disc. This is the case for the high/soft state of

4U1630 observed by *IXPE*, but the polarization is far larger than predicted by these models. This motivates our exploration of the contribution to the polarization signal from electron scattering in the accretion disc wind, which is clearly seen in this source. However, here we show that the optically thin wind produces a scattered flux with polarization in the opposite direction to that of the intrinsic optically thick disc emission, so the wind *depolarizes* the total spectrum. Hence, adding the wind to the optically thick disc cannot help explain the observed level of polarization. Yet the wind is clearly present, so its scattered flux must contribute. It is fairly easy to depolarize the optically thick disc through Faraday rotation from turbulent magnetic fields, but the wind alone predicts a polarization signal that is too small (Fig. 7), and too constant as a function of energy. It seems that the only way to get the observed high level of polarization is if the intrinsic optically thick disc can somehow be polarized in the opposite direction to the simple electron-scattering expectations. Quite how to do this remains unclear, but the answer may lie in anisotropic electrons in the photosphere (Krawczynski et al. 2023).

## ACKNOWLEDGEMENTS

We thank Henric Krawczynski for useful discussions. RT and CD acknowledge support from the STFC consolidated grant ST/T000244/1. CD thanks the Lorentz Centre for hosting a meeting on ‘Overcoming disconnects in black hole binaries’, which provided motivation to explore the polarization properties of winds, and thanks Kavli IPMU for visiting support. Numerical computations were in part carried out on Cray XC50 at Center for Computational Astrophysics (CfCA), National Astronomical Observatory of Japan (NAOJ). Numerical analyses were in part carried out on analysis servers at CfCA, NAOJ.

## DATA AVAILABILITY

The *NICER* data are publicly available. Access to the radiation transfer code is available on reasonable request to HO (odaka@ess.sci.osaka-u.ac.jp).

## REFERENCES

- Allen J. L., Schulz N. S., Homan J., Neilsen J., Nowak M. A., Chakrabarty D., 2018, *ApJ*, 861, 26
- Angel J. R. P., 1969, *ApJ*, 158, 219
- Begelman M. C., McKee C. F., Shields G. A., 1983, *ApJ*, 271, 70
- Capitanio F. et al., 2023, *ApJ*, 943, 129
- Chandrasekhar S., 1960, *Radiative Transfer*, Dover Press, New York
- Connors P. A., Piran T., Stark R. F., 1980, *ApJ*, 235, 224
- Davis S. W., Done C., Blaes O. M., 2006, *ApJ*, 647, 525
- Díaz Trigo M., Migliari S., Guainazzi M., 2014, *A&A*, 76, 1
- Done C., Gierliński M., 2005, *MNRAS*, 364, 208
- Done C., Tomaru R., Takahashi T., 2018, *MNRAS*, 473, 838
- Dovčiak M., Mulieri F., Goosmann R. W., Karas V., Matt G., 2008, *MNRAS*, 391, 32
- Dovčiak M., Steiner J. F., Krawczynski H., Svoboda J., 2023, *Astron. Telegram*, 16084, 1
- Gatuzz E., Díaz Trigo M., Miller-Jones J. C. A., Migliari S., 2019, *MNRAS*, 482, 2597
- Gianolli V. E. et al., 2023, *MNRAS*, 523, 4468
- Hori T., Ueda Y., Done C., Shidatsu M., Kubota A., 2018, *ApJ*, 869, 183
- Kastra J. S., Mewe R., Nieuwenhuijzen H., 1996, in *UV and X-ray Spectroscopy of Astrophysical and Laboratory Plasmas*, p. 411
- Kalemcı E., Maccarone T. J., Tomsick J. A., 2018, *ApJ*, 859, 88
- Krawczynski H. et al., 2022, *Science*, 378, 650

- Krawczynski H., Yuan Y., Chen A. Y., Rodriguez Cavero N., Hu K., Gau E., Steiner J. F., Dovčiak M., 2023, preprint ([arXiv:2307.13141](https://arxiv.org/abs/2307.13141))
- Kubota A. et al., 2007, *PASJ*, 59, S185
- Kubota M., Odaka H., Tamagawa T., Nakano T., 2018, *ApJ*, 868, L26
- Kushwaha A., Jayasurya K. M., Agrawal V. K., Nandi A., 2023, *MNRAS*, 524, L15
- Kuulkers E., Wijnands R., Belloni T., Méndez M., van der Klis M., van Paradijs J., 1998, *ApJ*, 494, 753
- Mahmoud R. D., Done C., 2020, *MNRAS*, 491, 5126
- Mao J., Kaastra J. S., Mehdipour M., Raassen A. J. J., Gu L., Miller J. M., 2017, *A&A*, 607, A100
- Matt G., Feroci M., Rapisarda M., Costa E., 1996, *Radiat. Phys. Chem.*, 48, 403
- Mikusincova R., Dovciak M., Bursa M., Lalla N. D., Matt G., Svoboda J., Taverna R., Zhang W., 2023, *MNRAS*, 519, 6138
- Neilsen J., Coriat M., Fender R., Lee J. C., Ponti G., Tzioumis A. K., Edwards P. G., Broderick J. W., 2014, *ApJ*, 784, L5
- Odaka H., Aharonian F., Watanabe S., Tanaka Y., Khangulyan D., Takahashi T., 2011, *ApJ*, 740, 103
- Odaka H., Khangulyan D., Tanaka Y. T., Watanabe S., Takahashi T., Makishima K., 2014, *ApJ*, 780, 38
- Ponti G., Fender R. P., Begelman M. C., Dunn R. J. H., Neilsen J., Coriat M., 2012, *MNRAS*, 422, L11
- Ratheesh A. et al., 2023, preprint ([arXiv:2304.12752](https://arxiv.org/abs/2304.12752))
- Rawat D., Garg A., Méndez M., 2023a, *MNRAS*, 525, 661
- Rawat D., Garg A., Méndez M., 2023b, *ApJ*, 949, L43 (R23)
- Rodriguez Cavero N. et al., 2023, *ApJ*, 958, L8
- Shidatsu M., Done C., 2019, *ApJ*, 885, 112
- Sugimoto J., Mihara T., Kitamoto S., Matsuoka M., Sugizaki M., Negoro H., Nakahira S., Makishima K., 2016, *PASJ*, 68, S17
- Sunyaev R. A., Titarchuk L. G., 1985, *A&A*, 143, 374 (ST85)
- Tomaru R., Done C., Ohsuga K., Nomura M., Takahashi T., 2019, *MNRAS*, 490, 3098
- Tomaru R., Done C., Ohsuga K., Odaka H., Takahashi T., 2020a, *MNRAS*, 494, 3413
- Tomaru R., Done C., Ohsuga K., Odaka H., Takahashi T., 2020b, *MNRAS*, 497, 4970
- Tomaru R., Done C., Mao J., 2023a, *MNRAS*, 518, 1789
- Tomaru R., Chris D., Odaka H., Tanimoto A., 2023b, *MNRAS*, 523, 3441
- Tomsick J. A., Lapshov I., Kaaret P., 1998, *ApJ*, 494, 747
- Trueba N., Miller J. M., Kaastra J., Zoghbi A., Fabian A. C., Kallman T., Proga D., Raymond J., 2019, *ApJ*, 886, 104
- Ursini F. et al., 2023, *A&A*, 676, A20
- Veledina A. et al., 2023, preprint ([arXiv:2303.01174](https://arxiv.org/abs/2303.01174))
- Weisskopf M. C. et al., 2016, in den Herder J.-W. A., Takahashi T., Bautz M., eds, Proc. SPIE Conf. Ser. Vol. 9905, Space Telescopes and Instrumentation 2016: Ultraviolet to Gamma Ray. SPIE, Bellingham, p. 990517
- Zdziarski A. A., Veledina A., Szanecki M., Green D. A., Bright J. S., Williams D. R. A., 2023, *ApJ*, 951, L45

This paper has been typeset from a  $\text{\TeX}/\text{\LaTeX}$  file prepared by the author.